

**Science**

 AAAS

**Dislocation Mean Free Paths and Strain Hardening  
of Crystals**

B. Devincere, *et al.*  
*Science* **320**, 1745 (2008);  
DOI: 10.1126/science.1156101

***The following resources related to this article are available online at  
www.sciencemag.org (this information is current as of June 27, 2008 ):***

**Updated information and services**, including high-resolution figures, can be found in the online version of this article at:

<http://www.sciencemag.org/cgi/content/full/320/5884/1745>

**Supporting Online Material** can be found at:

<http://www.sciencemag.org/cgi/content/full/320/5884/1745/DC1>

This article **cites 15 articles**, 3 of which can be accessed for free:

<http://www.sciencemag.org/cgi/content/full/320/5884/1745#otherarticles>

This article appears in the following **subject collections**:

Materials Science

[http://www.sciencemag.org/cgi/collection/mat\\_sci](http://www.sciencemag.org/cgi/collection/mat_sci)

Information about obtaining **reprints** of this article or about obtaining **permission to reproduce this article** in whole or in part can be found at:

<http://www.sciencemag.org/about/permissions.dtl>

2. J. W. Horton Jr., D. S. Powars, G. S. Gohn, Eds., *U.S. Geol. Surv. Prof. Pap. 1688* (2005).
3. C. Koeberl, C. W. Poag, W. U. Reimold, D. Brandt, *Science* **271**, 1263 (1996).
4. A. Deusch, C. Koeberl, *Meteorit. Planet. Sci.* **41**, 689 (2006).
5. G. S. Collins, K. Wünnemann, *Geology* **33**, 925 (2005).
6. G. S. Gohn *et al.*, *Eos* **87**, 349 (2006).
7. J. W. Horton Jr. *et al.*, *Geol. Soc. Am. Abstr. Prog.* **39**, 451, abstract 167-5 (2007).
8. J. W. Horton Jr., J. N. Aleinikoff, M. J. Kunk, C. W. Naeser, N. D. Naeser, *U.S. Geol. Surv. Prof. Pap. 1688* (2005).
9. P. B. Robertson, R. A. F. Grieve, in *Impact and Explosion Cratering: Planetary and Terrestrial Implications*, D. J. Roddy, R. O. Pepin, R. B. Merrill, Eds. (Pergamon, New York, 1977), pp. 687–702.
10. A. Wittmann, T. Kenkmann, L. Hecht, D. Stöffler, *Geol. Soc. Am. Bull.* **119**, 1151 (2007).
11. D. Stöffler *et al.*, *Meteorit. Planet. Sci.* **39**, 1035 (2004).
12. T. Hayden *et al.*, *Geology* **36**, 327 (2008).
13. D. S. Powars, T. S. Bruce, *U.S. Geol. Surv. Prof. Pap. 1612* (1999).
14. K. G. Miller, G. S. Mountain, Leg 150 Shipboard Party, Members of the New Jersey Coastal Plain Drilling Project, *Science* **271**, 1092 (1996).
15. K. G. Miller *et al.*, *Science* **310**, 1293 (2005).
16. J. V. Browning *et al.*, *Geol. Soc. Am. Bull.* **118**, 657 (2006).
17. D. S. Powars, *U.S. Geol. Surv. Prof. Pap. 1622* (2000).
18. C. W. Poag, *The Chesapeake Invader* (Princeton Univ. Press, Princeton, NJ, 1999).
19. E. R. McFarland, T. S. Bruce, *U.S. Geol. Surv. Prof. Pap. 1688-K* (2005).
20. W. E. Sanford *et al.*, *Eos* **85**, 369 (2004).
21. W. E. Sanford, *J. Geochem. Explor.* **78–79**, 243 (2003).
22. W. E. Sanford, *Geofluids* **5**, 185 (2005).
23. See supporting material on Science Online.
24. L. Radford, L. B. Cobb, R. L. McCoy, *U.S. DOE Rep. DOE/ET/28373-1* (1980).
25. F. T. Manheim, M. K. Horn, *Southeast. Geol.* **9**, 215 (1968).
26. A. L. Gronstal *et al.*, *Geol. Soc. Am. Abstr. Prog.* **39**, 316, abstract 116-22 (2007).
27. R. J. Parkes *et al.*, *Nature* **371**, 410 (1994).
28. S. D'Hondt *et al.*, *Science* **306**, 2216 (2004).
29. R. J. Parkes, B. A. Cragg, P. Wellsbury, *Hydrogeol. J.* **8**, 11 (2000).
30. W. D. Grant, *Philos. Trans. R. Soc. London Ser. B* **359**, 1249 (2004).
31. M. L. Maliniconico, W. E. Sanford, J. W. Horton Jr., abstract for Conference on Large Meteorite Impacts and Planetary Evolution IV, Vredefort Dome, South Africa, abstract 3068 (2008).
32. K. Kashafi, D. R. Lovley, *Science* **301**, 934 (2003).
33. The International Continental Scientific Drilling Program, the U.S. Geological Survey, and the NASA Science Mission Directorate provided funding for the drilling project. NSF and the Austrian Science Foundation provided supplementary funding for the drill-site operations. DOSECC Inc. conducted the administrative and operational management of the deep drilling project. We thank the Buyrn family for use of their land as a drilling site, the scientific and technical staff of the Chesapeake Bay Impact Structure Drilling Project for their many contributions, A. Gronstal (Open University, UK) for the microbe enumeration data, L. Edwards (USGS) for discussions of the post-impact geology, and G. Collins (Imperial College, UK) and K. Wünnemann (Humboldt-University Berlin) for making available the results of their numerical modeling.

### Supporting Online Material

www.sciencemag.org/cgi/content/full/320/5884/1740/DC1

Materials and Methods

Figs. S1 to S10

Table S1

References

4 April 2008; accepted 28 May 2008

10.1126/science.1158708

## REPORTS

# Dislocation Mean Free Paths and Strain Hardening of Crystals

B. Devincze,<sup>1</sup> T. Hoc,<sup>2</sup> L. Kubin<sup>1\*</sup>

Predicting the strain hardening properties of crystals constitutes a long-standing challenge for dislocation theory. The main difficulty resides in the integration of dislocation processes through a wide range of time and length scales, up to macroscopic dimensions. In the present multiscale approach, dislocation dynamics simulations are used to establish a dislocation-based continuum model incorporating discrete and intermittent aspects of plastic flow. This is performed through the modeling of a key quantity, the mean free path of dislocations. The model is then integrated at the scale of bulk crystals, which allows for the detailed reproduction of the complex deformation curves of face-centered cubic crystals. Because of its predictive ability, the proposed framework has a large potential for further applications.

Dislocations are complex defects of crystalline materials, which have been investigated for more than 70 years. Their fundamental and economical importance arises from the number of properties they govern, such as the high strength of nanostructured materials, the reliability of semiconductor devices, the processing and service life of structural materials, or the rheological properties of tectonic events in Earth's crust.

The irreversible, or plastic, deformation of crystals results from the motion on crystallographic planes of linear defects, the dislocations (1, 2). These defects carry an elementary amount of shear (the Burgers vector) that is usually the smallest

translation of the crystal lattice. During plastic flow, dislocations multiply and their mutual interactions hinder their motion. As a consequence, a shear stress increase  $d\tau$  has to be imposed to produce a shear strain increase  $d\gamma$ . By definition, the ratio  $d\tau/d\gamma$  is the strain hardening rate. Although dislocation theory has successfully explained many aspects of the strength of crystalline solids, predicting strain hardening is "the most difficult remaining problem" (3). The present dislocation-based models for strain hardening still have difficulties integrating elementary dislocation properties into a continuum description of bulk crystals or polycrystals. As a consequence, current approaches cannot avoid making use of extensive parameter fitting.

The present work takes advantage of three-dimensional dislocation dynamics (DD) simulations (4–8) for averaging dislocation properties at the intermediate scale of slip systems, which are ensembles of dislocations having the same Burgers vector and slip plane. The use of periodic boundary conditions allows for the tailoring of large dis-

location glide paths and the investigation of volumes that are representative of the bulk material (4). One can then derive a continuum formulation on the basis of physically justified mechanisms and parameters, and this formulation is further integrated at the scale of a bulk crystal. Face-centered cubic (fcc) crystals are taken as benchmark materials because of their well-documented, but rather complicated, stress/strain response.

We started by considering the critical stress  $\tau_c^i$  for the activation of slip system  $i$  as a function of the dislocation densities  $\rho^j$  stored (i.e., temporarily or permanently immobilized) in all slip systems  $j$ . This critical stress is given by a generalized Taylor relation (9) of the form,  $\tau_c^i = \mu b \sqrt{\sum_j a_{ij} \rho^j}$ ,

where  $\mu$  is the shear modulus and  $b$  the modulus of the Burgers vector. In fcc crystals, the symmetric tensor  $a_{ij}$  contains six independent dimensionless coefficients, which account for the average strength of pair interactions between slip systems that result from short- and long-range interactions. Their values were recently determined from DD simulations (5).

For determining strain hardening, the key quantity is the rate at which the critical stress evolves with strain or, equivalently, the rate at which dislocations accumulate under strain. For this purpose, it is useful to define a dislocation mean free path  $L$ , which is the distance traveled by a dislocation segment of length  $l$  before it is stored by interaction with the microstructure. When the line moves by a distance  $dx$ , it sweeps an area  $l dx$  and produces a shear strain  $d\gamma = b l dx / V$ , where  $V$  is the volume of the crystal. The stored density has then statistically increased by  $d\rho = (dx/L)/V$ , and the incremental storage rate is  $d\rho/d\gamma = 1/bL$ . This definition is only valid in differential form, as dislocation lines multiply when they move. Following Kocks *et al.* and

<sup>1</sup>Laboratoire d'Etude des Microstructures, Unité Mixte de Recherche (UMR) 104 CNRS, CNRS-Office National d'Etudes et de Recherches Aéronautiques (ONERA), 20 Avenue de la Division Leclerc, BP 72, 92322 Chatillon Cedex, France. <sup>2</sup>Laboratoire MSSMat, UMR 8579 CNRS, Ecole Centrale Paris, Grande Voie des Vignes, 92295 Chatenay-Malabry Cedex, France.

\*To whom correspondence should be addressed. E-mail: ladislav.kubin@onera.fr

Teodosiu *et al.* (10, 11), the net storage rate in each slip system  $i$  is written as

$$\frac{dp^i}{d\gamma^i} = \frac{1}{b} \left( \frac{1}{L^i} - \gamma p^i \right) \quad (1)$$

The last term at the right-hand side, where  $\gamma$  is proportional to the critical annihilation distance for screw dislocations, describes the effect of a mechanism called dynamic recovery (4). The mean free path  $L^i$  also appears in Eq. 1. Very little is presently known about the way  $L^i$  depends on dislocation interactions, stress, and specimen orientation.

At a small scale, plastic flow is not continuous but exhibits intermittency, as has been shown in several recent studies (12, 13). Figure 1A, which is extracted from a DD simulation, illustrates that the

unzipping of a single junction initiates several successive bursts of dislocation motion and expansion. As a consequence, the stored dislocation density increases in a discontinuous but progressive manner during straining (Fig. 1B), thus inducing strain hardening. Figure 1C shows the probability distribution functions of plastic strain-burst amplitudes,  $P(\delta\gamma_p)$ , as obtained from three DD simulations performed with different loading axes. For each orientation, a power law  $P(\delta\gamma_p) \sim \delta\gamma_p^{-\eta}$  is obtained in a bounded domain of amplitudes, with a scaling exponent  $\eta \approx 1.6$  in the range of previously measured values (12, 13).

Because the shear strain is the area swept by dislocations divided by the volume of the deforming crystal, these dislocation avalanches cannot be observed on the stress/strain curves of bulk crys-

tals. This suggests that a continuous description of uniform storage events through a coarse-graining procedure that smoothens out intermittency can be established. To ensure compatibility between the discrete and continuum approaches of storage, the parameters involved in the continuum approach discussed below are estimated as averages over the fluctuating output of DD simulations.

The most important contribution to the mean free paths arises from the interactions of moving dislocations with “forest” dislocations (that is, dislocations of other systems that pierce their slip plane) and their subsequent storage. We examined conditions such that  $n$  slip systems are active, with  $n > 1$ , and we considered one active slip system  $i$ . We made a simplifying assumption by replacing the interaction coefficients between slip systems

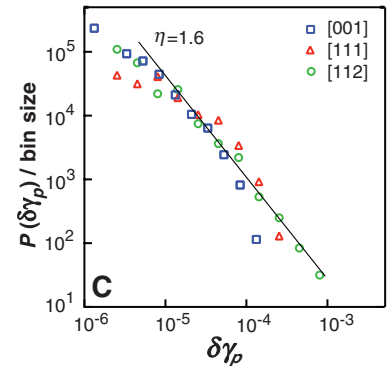
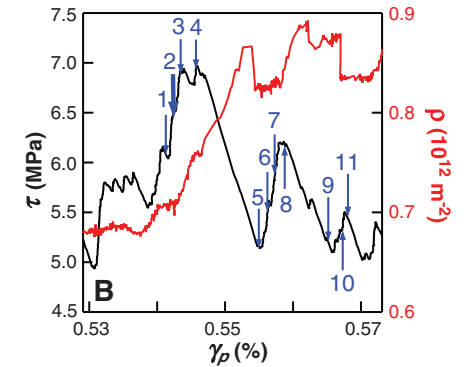
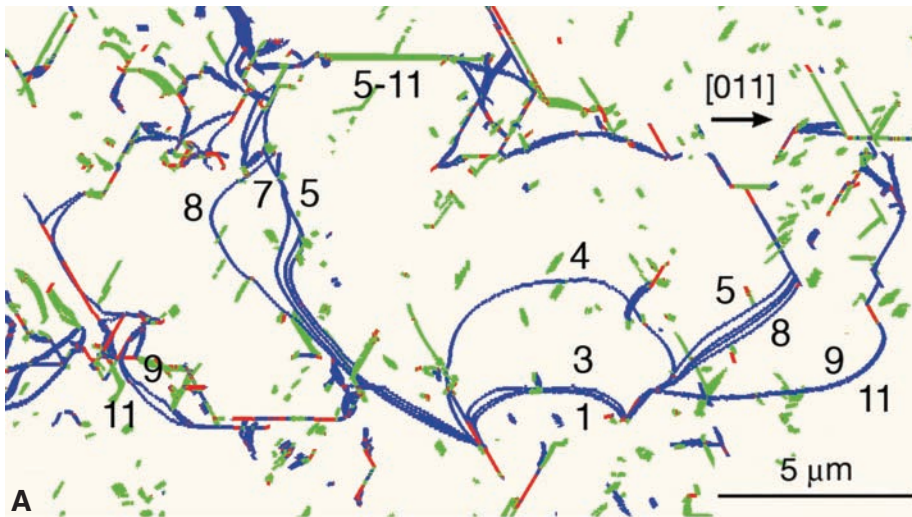


**Fig. 1.** Strain bursts during large-scale DD simulations of tensile deformation in copper crystals. The elementary simulation cell has a size of 4.4-by-4.9-by-5.9- $\mu\text{m}^3$ , the imposed strain rate is  $10 \text{ s}^{-1}$ , and periodic boundary conditions were used (4). (A) Successive dislocation avalanches occurring in the slip system  $s = [011](\bar{1}\bar{1}\bar{1})$  of a deforming  $[001]$  crystal. Superimposed configurations taken at constant time intervals are shown in a thin film of thickness =  $0.25 \mu\text{m}$  containing the active set of  $(\bar{1}\bar{1}\bar{1})$  extended slip planes. The forest slip systems (short green lines) form junctions (red straight lines) with the active slip system (blue lines). During its expansion, the unpinned segment (1) sweeps an area of  $\sim 130 \mu\text{m}^2$  before being stored again at dense forest tangles. (B) Corresponding evolutions of the resolved stress ( $\tau$ ) and dislocation density ( $\rho$ ) in  $s$  versus the total shear strain ( $\gamma_p$ ). Each jerk results from an avalanche, and arrows mark the dislocation configurations shown in (A). (C) Probability  $P(\delta\gamma_p)$  per bin size of the strain-burst amplitudes  $\delta\gamma_p$  for three simulations with high-symmetry orientations.

(C) Probability  $P(\delta\gamma_p)$  per bin size of the strain-burst amplitudes  $\delta\gamma_p$  for three simulations with high-symmetry orientations.

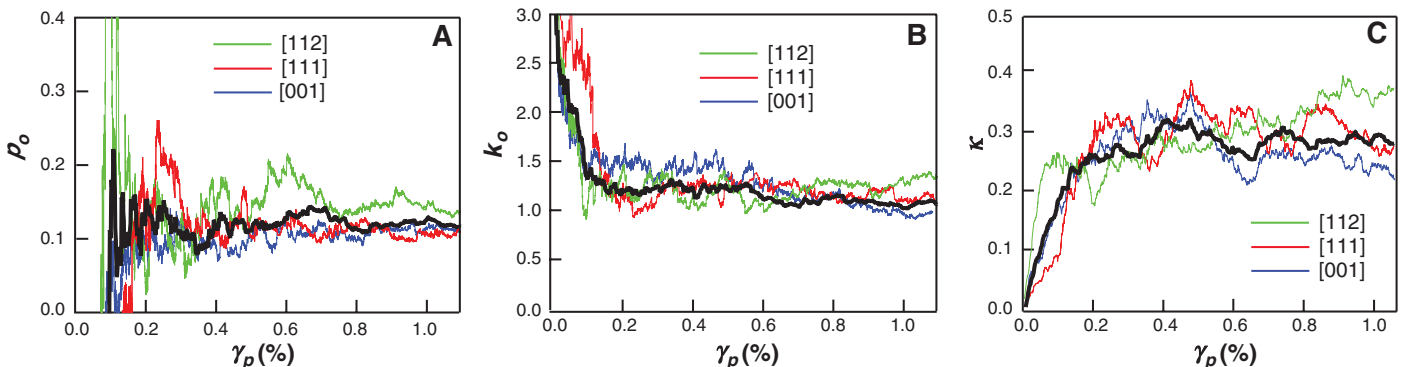


**Fig. 2.** Measurement of the dimensionless constants  $\rho_0$  (A),  $k_0$  (B), and  $\kappa$  (C) as a function of plastic shear strain by large-scale DD simulations and for three symmetrical orientations. Black lines represent the mean values. The elementary cell size is about  $(5 \mu\text{m})^3$ , and the imposed strain rate is  $\dot{\gamma} = 10 \text{ s}^{-1}$ .

$a_{ij}$  by their average value  $\bar{a}$ . During a time interval  $dt$ , mobile dislocations in  $i$  sweep an area  $dS^i$  and produce a strain increment  $d\gamma^i = bdS^i$  per unit of volume. The increase in stored density  $d\rho^i$  is the product of the number of stable junctions formed during a time increment and the dislocation density stored per junction.

The number of stable junctions formed during  $dt$  is the product of two terms. The first one is the number of intersections,  $dN_{\text{int}}$ , of mobile dislocations with the forest dislocations of  $i$ , in density  $\rho_f^i$  (where  $f$  refers to the forest). This quantity is proportional to  $\rho_f^i$  and to the swept area; hence,  $dN_{\text{int}} = \rho_f^i d\gamma^i/b$ . The second term incorporates the fact that not all intersections produce stable junctions (Fig. 1A). Because the stability of a junction is proportional to the average strength of the forest interactions (5), it is written in the form  $p_0\sqrt{\bar{a}}$ , where  $p_0$  is a constant.

The density stored by each junction is given by  $\bar{\ell}^i/V$ , where  $\bar{\ell}^i$  is the average length of the stored segments. As usual in dislocation theory, this length is inversely proportional to stress, and one has  $\bar{\ell}^i = k_0\mu b/\tau_c^i$ , where  $k_0$  is a dimensionless constant. However, one has to account for the contribution of junctions to the average lengths. Although junction lines do not necessarily share the attributes of perfect dislocations, they are redistributed into the densities stored in the active slip systems. This way, they can further react with mobile segments to form second-order junctions (6). As a result, one defines a last constant parameter, the ratio of junction density to total density in each slip system,  $\kappa$ .

Collecting all terms, one eventually obtains the storage rate per active slip system or, equivalently, the inverse of the mean free path (Eq. 1). The latter takes a relatively simple form in the case of loading along symmetrical orientations like [001], [111], or [112] when  $n$  active slip systems ( $n = 4, 3, 2$ , respectively) equally contribute to the total strain. One then has

$$\frac{1}{L^i} = \frac{\tau_c^i}{\mu b K_{hkl}}, \text{ with} \quad K_{hkl} = \left[ \frac{n(1+\kappa)^{3/2}}{p_0 k_0 \sqrt{\bar{a}}(n-1-\kappa)} \right] \quad (2)$$

This mean free path exhibits interesting properties that are also present in more general conditions. From Eq. 2, one can see that it is inversely proportional to the Taylor stress. It is also proportional to an orientation-dependent coefficient  $K_{hkl}$ , which depends on the three dimensionless constants ( $p_0$ ,  $k_0$ , and  $\kappa$ ) and also on the number  $n$  of active slip systems. In short, as  $n$  increases, the forest density seen by each active slip system increases too, and the mean free path decreases. Because  $n$  depends on the orientation  $[h,k,l]$  of the loading axis, an orientation dependence of the mean free path arises, which was not consistently modeled to date.

The constants defining the mean free paths were evaluated from two sets of independent DD simulations carried out with copper as a model material (4): (i) model simulations, in which a mobile slip system interacts with an immobile forest slip

system, and (ii) large-scale simulations of tensile deformation tests along three symmetrical axes, [112], [111], and [001]. Figure 2 illustrates the determination of the constants  $p_0$ ,  $k_0$ , and  $\kappa$  by large-scale simulations. Table 1 gives average values for the constants in Eq. 2, as obtained from the two sets of DD simulations. The values of the mean free path coefficients,  $K_{hkl}$ , can then be compared to the ones predicted by Eq. 2.

From the values of  $p_0$  and  $\kappa$ , one can infer that the fraction of attractive intersections that result in junction formation is  $\sim 25\%$ , whereas the average density of junctions is  $\sim 30\%$  of the total density in symmetrical conditions. The simulated and calculated values for  $K_{112}$  and  $K_{111}$  are in good agreement with one another. The difference between the values for  $K_{001}$  actually results from a particular dislocation mechanism that is specific to the [001] orientation (14). We used the measured value of  $K_{001}$  to correct the prediction of the model in that case.

Storage by forest interactions and Taylor hardening constitutes the two major building blocks for modeling strain hardening. Other building blocks are discussed in the supporting online material text. They are essentially concerned with self-interaction mechanisms, which govern strain hardening in single slip conditions (14), and dynamic recovery, which is related to the thermally activated annihilation of screw dislocations by cross-slip. Because the annihilation distance  $y$  in Eq. 1 incorporates two poorly known factors, a reference value was estimated from an experimental stress/strain curve.

To allow for a comparison between the predicted and experimental mechanical responses of single crystals, a change in scale is performed from mesoscopic to macroscopic dimensions. For this purpose, use is made of a crystal plasticity code (4, 15), which is a specific type of finite element code that takes into account the crystallographic nature of dislocation glide, deformation conditions, and lattice rotations during plastic flow. We then integrated the set of dislocation-based equations on a meshed tensile specimen (fig. S1).

**Table 1.** Average values of the dimensionless constants for fcc crystals involved in Eq. 2 and their variance. The number of independent measurements is indicated in parentheses in the top row. The values of the mean free path coefficients  $K_{hkl}$  can be compared to the ones calculated from Eq. 2 (italic numbers in parentheses). For a resolved shear stress of 10 MPa in copper, these values are almost identical to those of the mean free paths expressed in microns.

$p_0$ (6)	$k_0$ (6)	$\kappa$ (9)	$K_{112}$ (3)	$K_{111}$ (3)	$K_{001}$ (3)
$0.117 \pm 0.012$	$1.08 \pm 0.005$	$0.291 \pm 0.015$	$10.42 \pm 0.4$ (11.87)	$7.29 \pm 1.6$ (7.38)	$4.57 \pm 0.3$ (6.21)

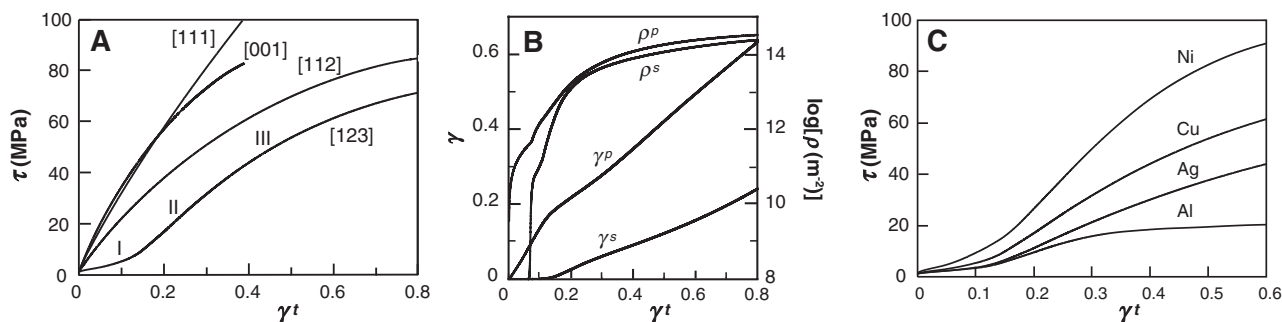


**Fig. 3.** Simulated mechanical response of fcc single crystals at room temperature.  $\tau$  and total strains ( $\gamma^t$ ) were drawn using traditional conventions for plotting experimental results. (A) Copper. Stress/strain curves were resolved on the primary slip system. Notice the strong orientation effect and the occurrence of three stages for the low-symmetry [123] orientation. The strain hardening rate increases from dissymmetrical double slip along [123] to symmetrical slip along [112], [111], and [001]; i.e., it increases with an increasing number of

active slip systems. The crossing of the [001] and [111] curves was experimentally observed. This crossing occurs because of a competition between the orientation dependencies of stages II and III. (B) Copper, [123] orientation. Densities ( $\rho$ ) and resolved strains ( $\gamma$ ) on the primary ( $p$ ) and secondary ( $s$ ) slip systems as a function of the total resolved strain, showing the transition between easy glide in stage I and forest hardening in stage II. (C) Resolved stress versus total shear strain curves for [123] Cu, Al, Ag, and Ni crystals at room temperature.

A selection of results is presented in Fig. 3 for tensile deformation at 300 K, with emphasis on copper crystals. Although the model does not incorporate ad hoc switches, the resolved stress/strain curves (Fig. 3A) exhibit the traditional stages that characterize fcc single crystals (16). The low-hardening stage I, during which a single slip system is activated, appears for low-symmetry orientations like [123]. The linear stage II is due to forest hardening, and its slope increases with the number of active slip systems. The subsequent decrease in strain hardening rate is also orientation-dependent and stems from dynamic recovery. All of these features are in excellent agreement with published experimental results (16, 17). Figure 3B shows the evolution of the shear strains and densities on the primary and secondary slip systems during a simulated [123] test. It is representative of the wealth of detailed information that can be obtained at the scale of slip systems. Finally, Fig. 3C illustrates a broader aspect of this type of modeling by presenting [123] stress/strain curves for several fcc crystals at room temperature. In addition to a rescaling of lattice parameters and elastic constants, shifting from one fcc material to the other implies changes in the annihilation properties of screw dislocations during dynamic recovery.

To address this, we tentatively used a scaling law derived from Escaig's model for cross-slip (4).

The present results indicate that, paradoxically, realistic strain hardening properties in uniaxial deformation are obtained without accounting for dislocation patterning (18, 19); that is, for the emergence of non-uniform microstructures during plastic flow. A possible reason is that the wavelength of dislocation patterns and the mean free path values follow the same scaling relation, in tension or compression.

This study shows that the mean free path of dislocations is the missing link connecting discrete dislocation interactions and avalanche processes to strain hardening properties in the bulk. The present multiscale methodology should apply to several areas of practical importance, such as the mechanical response of polycrystalline materials or size effects in small dimensions.

#### References and Notes

1. J. Friedel, *Dislocations* (Pergamon, Oxford, 1967).
2. J. Hirth, J. Lothe, *Theory of Dislocations* (Krieger, Malabar, FL, 1992).
3. A. H. Cottrell, in *Dislocations in Solids*, vol. 11, F. R. N. Nabarro, M. S. Duesbery, Eds. (Elsevier, Amsterdam, 2002), p. vii.
4. Simulation methods and additional information are available as supporting material on Science Online.

5. B. Devincere, L. Kubin, T. Hoc, *Scr. Mater.* **54**, 741 (2006).
6. V. V. Bulatov *et al.*, *Nature* **440**, 1174 (2006).
7. V. Bulatov, F. Abraham, L. Kubin, B. Devincere, S. Yip, *Nature* **391**, 669 (1998).
8. R. Madec, B. Devincere, L. Kubin, T. Hoc, D. Rodney, *Science* **301**, 1879 (2003).
9. P. Franciosi, M. Berveiller, A. Zaoui, *Acta Metall.* **28**, 273 (1980).
10. U. F. Kocks, H. Mecking, *Prog. Mater. Sci.* **48**, 171 (2003).
11. C. Teodosiu, J.-L. Raphanel, L. Tabourot, in *Large Plastic Deformations*, C. Teodosiu, J. L. Raphanel, F. Sidoroff, Eds. (A. A. Balkema, Rotterdam, Netherlands, 1993), p. 153.
12. M.-Carmen Miguel, A. Vespi gnani, S. Zapperi, J. Weiss, J.-R. Grasso, *Nature* **410**, 667 (2001).
13. F. F. Csikor, C. Motz, D. Weygand, M. Zaiser, S. Zapperi, *Science* **318**, 251 (2007).
14. B. Devincere, L. Kubin, T. Hoc, *Scr. Mater.* **57**, 905 (2007).
15. T. Hoc, C. Rey, J.-L. Raphanel, *Acta Mater.* **49**, 1835 (2001).
16. T. E. Mitchell, *Prog. Appl. Mater. Res.* **6**, 117 (1964).
17. T. Takeuchi, *Trans. JIM* **16**, 629 (1975).
18. L. Kubin, *Science* **312**, 864 (2006).
19. L. Kubin, B. Devincere, T. Hoc, *Mater. Sci. Eng. A* **483–484**, 19 (2008).
20. The authors acknowledge funding by their host institutions: CNRS, ONERA, and Ecole Centrale Paris.

#### Supporting Online Material

www.sciencemag.org/cgi/content/full/320/5884/1745/DC1

SOM Text

Fig. S1

References

5 February 2008; accepted 2 May 2008

10.1126/science.1156101

## Ordered Mesoporous Materials from Metal Nanoparticle–Block Copolymer Self-Assembly

Scott C. Warren,<sup>1,2</sup> Lauren C. Messina,<sup>2</sup> Liane S. Slaughter,<sup>2</sup> Marleen Kamperman,<sup>1</sup> Qin Zhou,<sup>2</sup> Sol M. Gruner,<sup>3</sup> Francis J. DiSalvo,<sup>2</sup> Ulrich Wiesner<sup>1\*</sup>

The synthesis of ordered mesoporous metal composites and ordered mesoporous metals is a challenge because metals have high surface energies that favor low surface areas. We present results from the self-assembly of block copolymers with ligand-stabilized platinum nanoparticles, leading to lamellar CCM-Pt-4 and inverse hexagonal (CCM-Pt-6) hybrid mesostructures with high nanoparticle loadings. Pyrolysis of the CCM-Pt-6 hybrid produces an ordered mesoporous platinum-carbon nanocomposite with open and large pores ( $\geq 10$  nanometers). Removal of the carbon leads to ordered porous platinum mesostructures. The platinum-carbon nanocomposite has very high electrical conductivity (400 siemens per centimeter) for an ordered mesoporous material fabricated from block copolymer self-assembly.

Despite considerable progress in the field of porous solids, major challenges remain in the synthesis of ordered mesoporous materials with high metal content from the coassembly of macromolecular surfactants and inorganic species. Controlling the structure of metals at the mesoscale (2 to 50 nm) is crucial for the development of improved fuel cell electrodes and may also assist in the miniaturization of optical and electronic materials for data transmission, storage, and computation (1, 2).

An early route to preparing mesoporous metals involves the dealloying of a less noble metal from a bimetallic alloy; this has been used for the prepara-

tion of Raney nickel and other metals (3). Dealloying processes provide limited control over structural parameters such as pore geometry and order. In contrast, block copolymer self-assembly or templating with metal species provides access to highly ordered structures. Synthetic routes to such structures have included adsorbing and then reducing metal ions within a preassembled block copolymer scaffold (4) and coassembling ligand-stabilized nanoparticles (NPs) with block copolymers (5). More recently, polymer-coated NPs that behave like surfactants have been isolated at the interface of block copolymer domains, which can create a bicontinuous morphology at higher loadings (6).

Despite this progress, the conversion of metal-polymer hybrids into mesoporous materials with ordered and large pores ( $\geq 10$  nm) has not been accomplished, in part because of the low volume fraction of metals in most hybrids and the widespread use of gold, which has a high diffusion coefficient and therefore retains its mesostructure only at low temperatures (7–9). Although a protective organic layer can be added to metal NPs to prevent uncontrolled aggregation, even a thin organic layer represents a considerable volume of the overall material: For example, a 1-nm-diameter metal NP with a relatively thin 1-nm organic shell is just 4% metal by volume. As a result, the typical metal content in most block copolymer–metal NP hybrids is only a few volume %, and the prospects for converting the hybrid into an ordered mesoporous material, in which the metal would have a volume fraction between 60 and 75% for an inverse hexagonal structure, are poor.

Mesoporous metals have been synthesized at a smaller length scale, with 2- to 4-nm pores, through the coassembly of metal ions with small-molecule surfactants followed by reduction (10–13). The small pore size, however, limits the flow of liquids through the material, which is essential for many applications (14, 15). Metals have also been deposited onto (16) or into (17) thin films of block

<sup>1</sup>Department of Materials Science and Engineering, Cornell University, Ithaca, NY 14853, USA. <sup>2</sup>Department of Chemistry and Chemical Biology, Cornell University, Ithaca, NY 14853, USA. <sup>3</sup>Department of Physics, Cornell University, Ithaca, NY 14853, USA.

\*To whom correspondence should be addressed. E-mail: ubw1@cornell.edu